

Effect of Surface Pressure on Oxygen Transfer across Molecular Monolayers at the Air/Water Interface: Scanning Electrochemical Microscopy Investigations Using a Mercury Hemispherical Microelectrode Probe

Ilenia Ciani,^{†,‡} David P. Burt,[†] Salvatore Daniele,[‡] and Patrick R. Unwin^{*,†}

Department of Chemistry, University of Warwick, Coventry CV4 7AL, U.K., and Department of Physical Chemistry, University of Venice, Calle Larga S. Marta, 2137, 30123 Venice, Italy

Received: August 4, 2003; In Final Form: January 23, 2004

Investigations of the kinetics of molecular transfer across the liquid/gas interface and the effect of a molecular monolayer are of considerable interest as a model for certain biological and environmental processes. In this work, a combined scanning electrochemical microscopy (SECM)–Langmuir trough technique has been used to investigate the effect of the chemical character and mechanical compression of molecular monolayers on the rate of oxygen transfer across the air/water (A/W) interface. Specifically, monolayers comprising the fatty alcohol 1-octadecanol and the phospholipid L- α -dipalmitoyl phosphatidic acid were considered. A mercury hemispherical microelectrode probe has been used to measure interfacial kinetics in SECM, and a numerical model has been developed for mass transport in this configuration to allow quantitative analysis of experimental data. The results obtained suggest that, for both monolayers, the oxygen-transfer rate across the interface decreased compared to that across the clean interface, with the blocking effect becoming more pronounced as the surface pressure of the monolayer increased. A simple energy-barrier model was used successfully to interpret the dependence of the rate constant of oxygen transfer on the surface pressure. The experimental data also provide evidence for the effect of the SECM probe on the deformation of the water surface at very close distances to the A/W interface.

Introduction

Understanding the transport of small molecules and ions across thin films and membranes is important in a wide range of areas¹ including the life sciences² and in environmental processes.³ The regulation of ion concentrations on the interior and exterior of a biological cell, for instance, controls the functioning of almost every cell. Other processes of physiological relevance in living cells include drug permeability and gaseous exchange across the membrane.

Passive diffusion is an important type of solute transport across membranes. This process governs not only the transport of small molecules (e.g., oxygen, water, urea, and formamide) but also the majority of common drugs and organic ions.⁴ This type of permeation plays a role in establishing osmotic balance,^{4a,5} and in some cases, there is also a specific biological role.⁶

A simple model of a lipid membrane is provided by a monolayer at the air/water (A/W) interface.^{7,8} The advantage of this model lies in the ability to control the properties of such interfaces readily by use of a Langmuir film balance. Specifically, it is possible to study the role of the molecular density and surface pressure, by varying the mean area per surface molecule, using this apparatus. In addition, investigations of a range of chemical properties of the film are feasible by changing the constituent amphiphatic molecule. Solute and solvent transfer across this type of interface has been the subject of many studies,⁹ following the first demonstration by Rideal¹⁰ that monolayers were effective in reducing water evaporation rates. However, quantitative investigations of the permeability of monolayers to solute molecules are somewhat rare.

Scanning electrochemical microscopy (SECM)¹¹ is proving to be a powerful technique for probing diffusion and reactivity at monolayers,¹² bilayers,¹³ and membranes.^{14,15} Interfacial dynamics and diffusion can be studied on small length and time scales approaching those relevant to cellular membranes. Particularly relevant to the work herein is the SECM induced-transfer (SECMIT) mode,¹⁶ which is one of a family of equilibrium perturbation-based approaches.¹⁷ This technique was recently applied in a Langmuir trough to study the effect of 1-octadecanol (denoted henceforth as C₁₈OH) on oxygen-transfer rates across an A/W interface.¹⁸ In recent applications to molecular assemblies at the A/W interface, SECM has been used to study lateral proton diffusion,¹⁹ the effect of fatty alcohol monolayers on the rate of bromine transfer across the A/W interface,²⁰ and lateral diffusion and charge-transfer processes.²¹

In this paper, we use the SECM method to study the kinetics of oxygen transfer across monolayers at an A/W interface. As mentioned above, we have reported preliminary work on oxygen transfer across C₁₈OH,¹⁸ but the data were analyzed using a simple accessible-area model,⁹ although more sophisticated models are available and may be more appropriate.²⁰ Here we not only investigate oxygen transfer across the more biologically relevant system of a phospholipid monolayer, specifically, L- α -dipalmitoyl phosphatidic acid (DPPA), but also consider the analysis of the data by means of an energy-barrier model for gas/liquid transfer, first suggested and developed by Langmuir and co-workers.²² This approach has previously proved successful in the interpretation of ion-transfer kinetics across monolayers at liquid/liquid interfaces^{12d,23} and Br₂ transfer across fatty alcohol monolayers.²⁰

The method we employ makes use of a submarine mercury hemispherical microelectrode as the SECM probe. This type of probe has recently been introduced into SECM²⁴ and may extend the types of species and processes that can be studied. It has

* Corresponding author. E-mail: P. R. Unwin@warwick.ac.uk. Fax: +44 2476524112. Phone: +44 2476523264.

[†] University of Warwick.

[‡] University of Venice.

not yet, however, been used to measure interfacial kinetics quantitatively. The use of a mercury electrode, in the present application, has several potential advantages over previous work using solid electrodes such as Pt. First, to detect oxygen transfer, we use the electroreduction of oxygen, which on mercury occurs in two distinct steps, producing hydrogen peroxide in an initial two-electron process and then hydroxide at more cathodic potentials. Thus, the potential can be tuned to avoid the production of hydroxide ions, thereby avoiding pH perturbation near the monolayer. This is particularly important in the present studies on DPPA, where changes in interfacial pH may alter the local charge density and organization of the monolayer.

Second, in these types of study, the microelectrode probe ultimately causes significant mechanical deformation to the W/A interface as it approaches.^{18–20} This part of the SECM approach curve has been neglected previously, and measurements have focused on the region of the curve where the water surface is unperturbed. We show here that such deformations, with a mercury hemispherical microelectrode, affect the behavior of the current–distance curves in a reproducible manner. Careful analysis of these curves allows the modeling of the deformation process in a detailed way for the first time. Finally, the use of mercury microelectrodes opens up the possibility of using anodic stripping voltammetry for future SECM studies on the interaction of metal ions (particularly heavy metals) with biomembranes. This is a subject of considerable interest,^{25–27} where measurements are presently difficult.

Experimental Section

Chemicals. All chemicals were used as received. The fatty alcohol was C₁₈OH (99%) (Aldrich), and the phospholipid was DPPA (99%) (Sigma). Other chemicals were chloroform (HPLC grade), methanol (BDH, AnalaR), mercurous nitrate (A. R. Fisons), potassium nitrate (99.99%) (Aldrich), and nitric acid (BDH, AnalaR). All aqueous solutions were prepared from Milli-Q reagent water (Millipore Corp.).

Apparatus. The Langmuir trough (model 611, Nima technology, Coventry, U.K.) was housed in a glovebox (Glovebox Technology, Huntingdon, U.K.). The microelectrode probe of the SECM was positioned using a set of *x*, *y*, *z* stages (M-462, Newport Corp., Irvine, CA) and a piezoelectric positioner and controller (models P843.30 and E-662, Physik Instrumente, Germany) to give fine remote positioning capabilities in the direction normal to the interface. Current–distance approach curves were recorded by translating the electrode from a position far from the interface (ca. 50 μm) toward the interface at a rate of 0.5 $\mu\text{m s}^{-1}$. The potential of the microelectrode was controlled using a voltage generator, and the current was measured with a current follower (built in-house). A bipotentiostat fitted with a low-current module (CH Instruments, Austin, TX, model 730A) was employed in the preparation of mercury microelectrodes.

Procedures. The procedure for the fabrication of the submarine microelectrode has been described previously.²⁸ The platinum microelectrode used for all of the measurements was a 25- μm -diameter disk, characterized by an *RG* value ($RG = b/a$, where *b* is the radius of the probe and *a* is the radius of the disk-shaped electrode)²⁹ of 10.

Mercury microelectrodes were prepared by the cathodic deposition of mercury onto the Pt microdisk in a deaerated solution containing 10 mM Hg₂(NO₃)₂, 0.5 M KNO₃, and 1% HNO₃, as reported elsewhere.³⁰ To produce a hemispherical electrode, the deposition was continued until the current value was $\pi/2$ times the initial value. The dimensions of the electrode were checked using optical microscopy (Olympus BH2 micro-

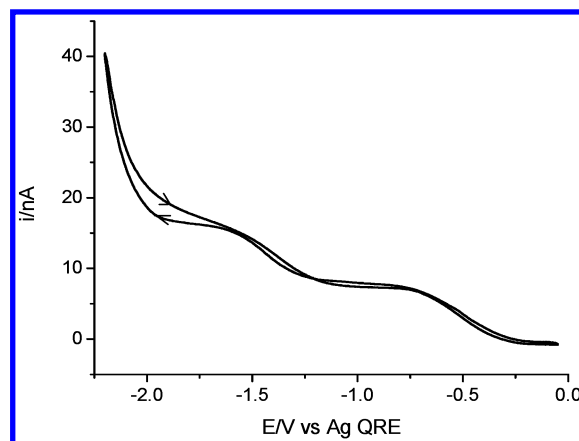


Figure 1. Voltammetry of oxygen reduction in 0.1 M KNO₃ aerated aqueous solution at a hemispherical mercury microelectrode. Scan rate: 5 mV s⁻¹.

scope). Electrochemical measurements were performed using a two-electrode arrangement, with a silver wire serving as a quasi-reference electrode (AgQRE).

To form the monolayers at the A/W interface in the Langmuir trough, 70 μL of a 0.9 mg/mL (1:4 (v/v) methanol/chloroform) DPPA solution or 60 μL of a 1 mg/mL (in chloroform) C₁₈OH solution was spread dropwise over the subphase (an aqueous solution containing 0.1 M KNO₃) using a microliter syringe (100- μL volume, Hamilton, Reno, NV). Chloroform was chosen as the spreading solvent for C₁₈OH because previous studies³¹ suggested that it was optimal for fatty alcohols: the loss of fatty alcohol monolayers into the subphase has been observed when ethanol is used as the spreading solvent.³² The solvent was allowed to evaporate for 15–20 min before any measurements were made. Pressure–area isotherms were typically recorded with a barrier speed of 25 cm² min⁻¹ from an initial surface area of 500 cm².

Results and Discussion

Preliminary Experiments. At mercury electrodes, oxygen reduction is a two-step reaction (Figure 1) with two electrons involved in each step. The steady-state diffusion-limited current at a hemispherical microelectrode for the first step (formation of H₂O₂) is given by

$$i_{\infty} = 2\pi nFDc^*a \quad (1)$$

In eq 1, *n* = 2 is the number of electrons transferred, *F* is Faraday's constant, *D* is the diffusion coefficient of O₂, and *c*^{*} = 2.5 × 10⁻⁴ mol dm⁻³ is the bulk concentration³³ of O₂. The experimental value of *i*_∞ was 8.0 ± 0.2 nA, yielding a value for the diffusion coefficient for O₂ of 2.1 × 10⁻⁵ cm² s⁻¹, in good agreement with previous measurements.^{33a}

SECM approach curves for O₂ reduction to H₂O₂, with the probe microelectrode approaching a clean A/W interface, in a solution containing 0.1 M KNO₃, were also used to characterize the Hg electrodes in the SECM configuration. Hg electrodes have been used previously in SECM for hindered diffusion measurements,²⁴ and the studies here allow other mass-transport models with a hemispherical electrode to be tested^{34–36} and also provide a baseline for the experiments that follow.

Figure 2 shows typical experimental results, compared with different theoretical predictions.^{34–36} It can be seen that the experimental current rises as the probe approaches the interface because the air phase provides an infinite source of O₂, so maintaining the concentration at the surface of the water subphase at the bulk value.¹⁸ To compare the experiment with

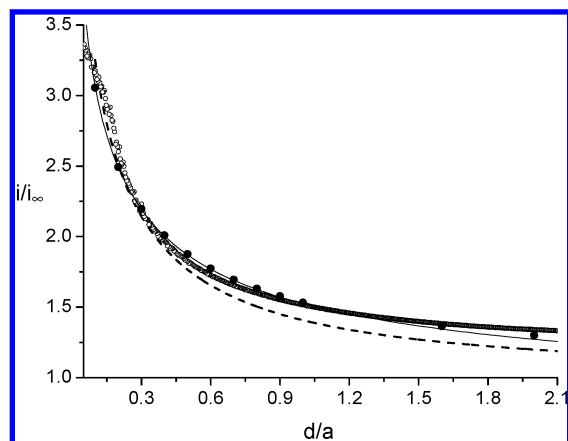


Figure 2. Experimental (○) and theoretical (●) (FEMLAB package), (—) from ref 34, (---) from refs 35 and 36, approach curves for the reduction of O_2 to H_2O_2 at a hemispherical microelectrode in a solution containing 0.1 M KNO_3 . Steady-state approach curves were measured by setting the tip potential to -0.9 V vs Ag QRE.

the various models, the distance of the microelectrode probe from the interface was needed. Given that O_2 transfer across this interface is known to be diffusion-limited on the SECM timescale with no limitations from the second (air) phase,¹⁸ the absolute tip–interface distance, d , was the only adjustable parameter in fitting the approach curves. This distance is conventionally defined as the closest separation between the surface of the hemispherical electrode and the flat interface. It can be seen that the prediction reported in ref 34 is in good agreement with the experimental data over most of the tip–interface separations of interest. Additionally, the results simulated (as described later) with the finite element method³⁷ by using the FEMLAB package (Comsol Group, Stockholm, Sweden) are also highly consistent with the data.

There is some deviation of the experimental data from theory at the closest distances, which is due to the deformation of the water surface by the approaching probe. The nature of this process will be discussed in more detail later in this paper.

An alternative theoretical response can be obtained by numerically evaluating the integral in eq 8 reported in ref 35, combined with eq 19 in ref 36. The agreement of this last prediction with our experimental data and the simulations of Selzer and Mandler³⁴ is less satisfactory. This may be expected because of the additional approximations involved in the derivation of this curve.

Effect of Monolayers on Oxygen Transfer across the A/W Interface. The relationship between surface pressure, Π , and area per molecule of both $C_{18}OH$ and DPPA is given in Figure 3. The shape of the isotherms and the characteristic parameters deduced from the figure (collapse pressure and corresponding area per molecule) were as expected.^{38–40} The collapse pressures were 49.5 and 50 mN/m, respectively, for DPPA and $C_{18}OH$, which lie within the range of collapse-pressure values reported previously.^{37b,c,38} The molecular area of DPPA at the collapse pressure was $38.7 \text{ \AA}^2/\text{molecule}$, which compares well with reported values.^{38a,d} It is also within the expected range for the cross-sectional area of two hydrocarbon chains. (For diacyl lipids with untitled vertical chains, the molecular area is between 36 and 42 \AA^2 .^{38e}) For $C_{18}OH$, the molecular area at the collapse pressure is $17.8 \text{ \AA}^2/\text{molecule}$, as expected.³⁹ This corresponds well with the alkyl chain cross-sectional area.⁴⁰

By using a hemispherical mercury microelectrode, families of approach curves for oxygen reduction were obtained at different surface pressures for $C_{18}OH$ and DPPA monolayers. Typical

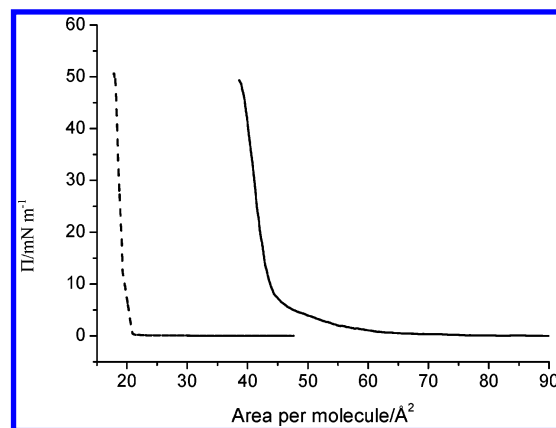


Figure 3. Π – A isotherms for 1-octadecanol (---) and DPPA (—) recorded with an aqueous subphase of 0.1 M KNO_3 at pH 5.4.

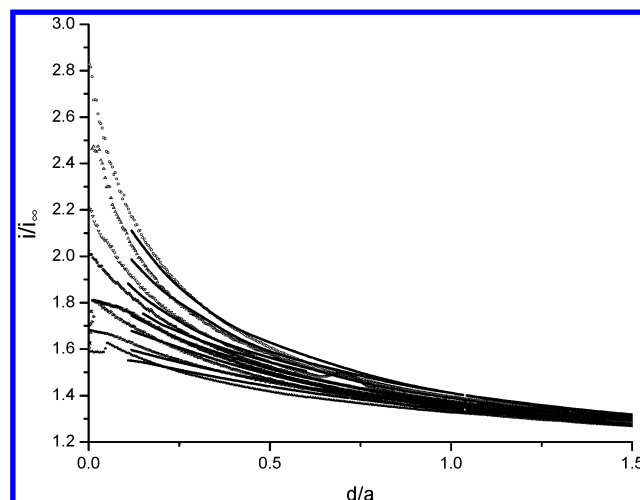


Figure 4. Normalized experimental approach curves (○, ▽, ▲) for oxygen reduction at a hemispherical microelectrode approaching an A/W interface for various $C_{18}OH$ monolayer pressures. From top to bottom, the curves correspond to uncompressed and surface pressures of 5, 10, 15, 20, 25, 30, and 40 mN/m. The solid lines (top to bottom) represent the theoretical behavior for $k_{w,a}/\text{cm s}^{-1} = 0.070, 0.043, 0.040, 0.039, 0.035, 0.032, 0.029$, and 0.026.

experimental results are shown in Figures 4 and 5. In both cases, it can be seen that as the surface pressure increases the flux of O_2 across the A/W interface decreases, as manifested in the diminution of the tip current. This demonstrates that an increasing interfacial resistance is introduced into the transfer process.

To model the data, the reduction of oxygen at the electrode surface was simulated using the FEMLAB package. Mass transport of O_2 to the microelectrode occurs via steady-state diffusion in the axisymmetric cylindrical geometry of the SECM:

$$D \left(\frac{\partial^2 c}{\partial r^2} + \frac{1}{r} \frac{\partial c}{\partial r} + \frac{\partial^2 c}{\partial z^2} \right) = 0 \quad (2)$$

where c is the concentration of O_2 in solution and r and z are the coordinates in the radial and normal directions, respectively, relative to the electrode surface with the origin at the center, as shown in Figure 6. The microelectrode was considered to be at a potential where oxygen reduction was under diffusive control, and the insulating glass sheath is inert, leading to the boundary conditions

$$z = \sqrt{(a^2 - r^2)} \quad r \leq a: c = 0 \quad (3)$$

$$z = 0 \quad a \leq r \leq r_{\text{glass}}: D \left(\frac{\partial c}{\partial z} \right) = 0 \quad (4)$$

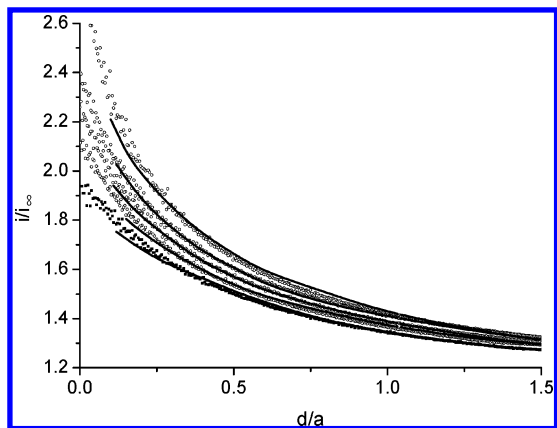


Figure 5. Selection of typical normalized experimental approach curves (○, ■) for oxygen reduction at a hemispherical microelectrode approaching an A/W interface for various DPPA monolayer pressures. From top to bottom, the curves correspond to uncompressed and surface pressures of 5, 10, 20, and 30 mN/m. The solid lines (top to bottom) represent the theoretical behavior for $k_{wa}/\text{cm s}^{-1} = 0.088, 0.060, 0.053, 0.049$, and 0.042 .

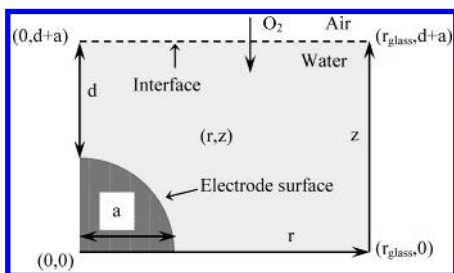


Figure 6. Schematic of the geometry for the simulation of the microelectrode—monolayer system, together with the coordinate system and notation.

where r_{glass} is the radial distance from the center of the electrode to the edge of the insulating glass sheath surrounding the electrode. In typical experimental practice, $r_{\text{glass}} \geq 10a$. Further boundary conditions define a zero radial flux at the center of symmetry, $r = 0$, and a bulk concentration of oxygen at the far edges of the simulation domain, defined by $r = r_{\text{glass}}$ and $z = d + a$:

$$a \leq z \leq (d + a) \quad r = 0: D \frac{\partial c}{\partial r} = 0 \quad (5)$$

$$0 \leq z \leq (d + a) \quad r = r_{\text{glass}}: c = c^* \quad (6)$$

For a clean interface, there are no limitations to O_2 transport across the A/W interface, and the boundary condition at the water surface is given by

$$z = (d + a) \quad 0 \leq r \leq r_{\text{glass}}: c = c^* \quad (7)$$

If the interface has a monolayer, then the corresponding boundary condition depends on the kinetics of the transfer of oxygen across the A/W interface, affected by the pressure change. The flux of oxygen from the air phase, $j_{\text{O}_2}/\text{mol cm}^{-2} \text{ s}^{-1}$, following first-order interfacial kinetics¹⁸ is given by

$$j_{\text{O}_2} = k_{aw}c_a - k_{wa}c_{wi} \quad (8)$$

where k_{wa} and $k_{aw}/\text{cm s}^{-1}$ are rate constants for the transfer of O_2 from water to air and from air to water, respectively. The interfacial concentration of oxygen in the water phase is c_{wi} , and c_a is the concentration of oxygen in the air, which is constant throughout the phase. At equilibrium,

TABLE 1: Measured Rate Constants $k_{wa}/\text{cm s}^{-1}$ for Oxygen Transfer at Different Values of Surface Pressure $\Pi/\text{N m}^{-1}$ for 1-Octadecanol and DPPA Monolayers

1-octadecanol		DPPA	
$\Pi/\text{N m}^{-1}$	$(k_{wa} \pm 0.0005)/\text{cm s}^{-1}$	$\Pi/\text{N m}^{-1}$	$(k_{wa} \pm 0.001)/\text{cm s}^{-1}$
0	0.070		
0.005	0.043	0	0.088
0.01	0.040	0.005	0.060
0.015	0.039	0.01	0.053
0.02	0.035	0.02	0.049
0.025	0.032	0.03	0.042
0.03	0.029	0.04	0.037
0.04	0.026		

$$k_{aw}c_a = k_{wa}c^* \quad (9)$$

so that eq 8 translates into the following final boundary condition:

$$z = d + a \quad 0 \leq r \leq r_{\text{glass}}: \frac{\partial c}{\partial z} = \frac{k_{wa}}{D}(c^* - c) \quad (10)$$

The simulations were carried out with all parameters normalized as described elsewhere.^{17,18} The best fits between experiment and simulation are shown in Figures 4 and 5, from which k_{wa} was obtained. Values of k_{wa} as a function of Π are summarized in Table 1. These data represent the mean values and standard deviation, obtained from the best fits to five approach curves (at each pressure), recorded on different days and with different monolayers to ensure reproducibility.

The relationship between k_{wa} and Π was tested by means of the energy-barrier model.²² Several groups^{41,42} have used and developed this model to explain experimental observations of the effect of monolayers on the evaporation of water. Recently, it was used successfully to interpret the effect of monolayer surface pressure on the transfer rate constant of bromine across the W/A interface²⁰ and the blocking effect of a phospholipid monolayer on IrCl_6^{2-} ion transfer across the water/1,2-dichloroethane interface.²¹

The energy-barrier model is based on a Boltzmann expression to give the fraction of molecules that have energy in excess of that needed to permeate a monolayer. On the assumption that the Gibbs free energy of activation for solute transfer is equal to the work required to open a pore of radius r_p in the monolayer, the general expression for the transfer rate constant is

$$k = B \exp\left(-\frac{\pi r_p^2 \Pi}{k_B T}\right) \quad (11)$$

where the preexponential function B embodies factors related to monolayer structure,⁴³ k_B is the Boltzmann constant, T is the absolute temperature, and r_p is the radius of the transferring species, in this case oxygen. It follows that a plot of $\ln(k)$ versus Π should be linear and that from the slope one should be able to find the radius of the pore.

The experimental data, together with this fit, are shown in Figure 7a for C_{18}OH and in Figure 7b for the DPPA monolayer. The resulting values for r_p are (1.4 ± 0.3) and (1.3 ± 0.4) Å, respectively. These values are in close agreement with the radius of molecular oxygen,⁴⁴ 1.2 Å.

Analysis of the Full Form of the SECM Approach Curves. The simulation data used for the analysis above reproduce the

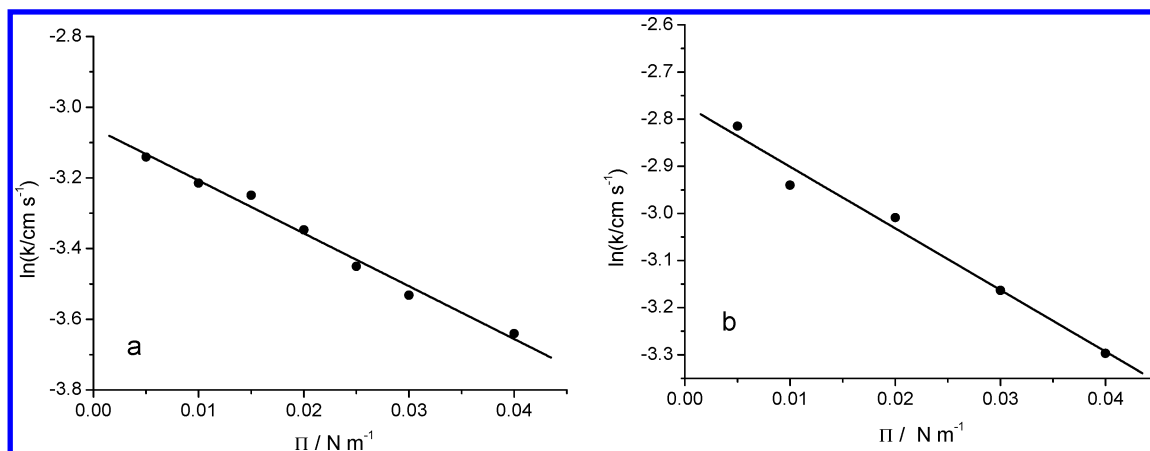


Figure 7. Dependence of the rate constant for oxygen transfer on surface pressure across (a) $C_{18}OH$ and (b) DPPA monolayers. The data are linearly fitted for analysis in terms of eq 11.

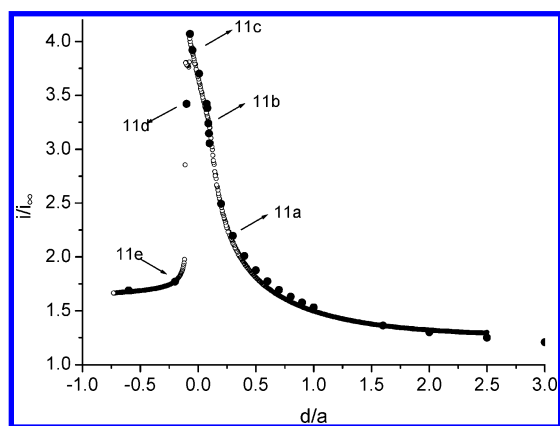


Figure 8. Experimental (○) and theoretical (FEMLAB) (●) approach curves for a hemispherical microelectrode approaching a clean A/W interface (via reduction of O_2 to H_2O_2) in a solution containing 0.1 M KNO_3 . The simulation is described in the text.

experimental approach curves down to $d/a = 0.1$. Below this value, the experimental curves, in the majority of cases, display a reproducible behavior that differs in form depending on whether the water surface is clean or has a monolayer. Typical approach curves for the cases of a clean interface and an interface with a monolayer at two surface pressures are shown in Figures 8 and 9, respectively.

The form of these curves can be explained by the fact that when the probe is close to the A/W interface the water surface becomes deformed and curved because of the perturbing action of the microelectrode tip. In particular, from the experimental

data and from direct observation with video microscopy of the approach of the microelectrode to the interface, it was possible to establish that this process involves two different steps. Each of these is characterized by a different curvature of the surface, depending on the relative position of the tip. Both steps identified are due to the interplay of the surface tension of the water surface with the changing constraints imposed by the moving electrode. First, the surface continuously bends because of the pushing motion of the tip toward the surface (Figure 10a). After that, the water curvature develops a discontinuity: it is concave above the electrode and convex below it (Figure 10b). The crossover between the two steps occurs at a value of d that depends strongly on the presence or absence of a monolayer (i.e., on the tension of the A/W interface).

It is to be noted that during these two steps the change in the shape of the interface means that the values of d/a no longer represent the real distance of the probe from the water surface. In particular, d/a can take negative values because we define it as the distance, with respect to the initially flat interface, so that it depends on the electrode movement, controlled by the piezoelectric positioner. The geometrical distances considered to model the experimental situation (see d and dl in Figure 11) are not related in a simple way to d/a because they are influenced by the surface tension and the resistance of the water interface to curvature. This means that the analysis that follows is semiquantitative.

Deformation at a Clean Water/Air Interface. Let us first consider the case in which there is no monolayer. A typical approach curve is shown in Figure 8. This shows three distinct

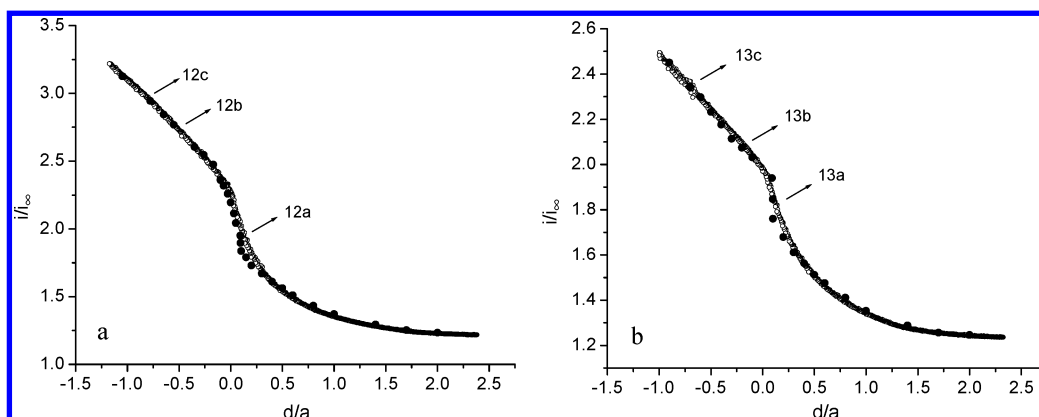


Figure 9. Experimental (○) and theoretical (FEMLAB) (●) approach curves for a hemispherical microelectrode inducing the transfer of O_2 across an A/W interface with a DPPA monolayer in a subphase containing 0.1 M KNO_3 . The monolayer pressure was (a) $\Pi = 10$ mN/m and (b) $\Pi = 30$ mN/m. The simulation is described in the text.

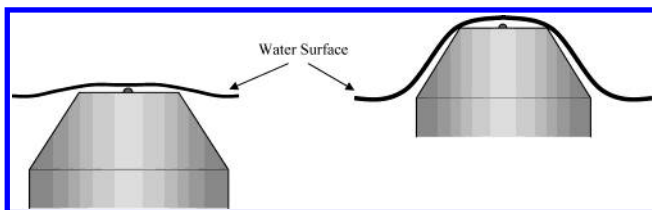


Figure 10. Schematic representation of the water surface as the microelectrode is pushed upward through an A/W interface. (Left) Initial stage of the deformation; (right) situation just before the emergence of the probe.

regimes. The first extends from bulk solution to $d/a = 0.1$ and was fitted as reported in Figure 2. The second regime corresponds to a sharp change in the slope of the approach curve,

which extends up to about $d/a = -0.1$. Third, we observed an abrupt drop in the recorded current, followed by a region in which it stayed almost constant up to $d/a = -1$.

In Figure 8, we also show the numerical results obtained with FEMLAB; the corresponding concentration profiles and geometries for the different stages of the liquid deformation are reported in Figure 11. The points corresponding to the second regime (Figure 11b and c) were calculated by considering that as the microelectrode was pushed upward the curvature of the surface became progressively sharper and the distance between the interface and tip, d , decreased from approximately $0.09a$ to $0.04a$. As a consequence, the current increases but less dramatically than would have been found without considering the

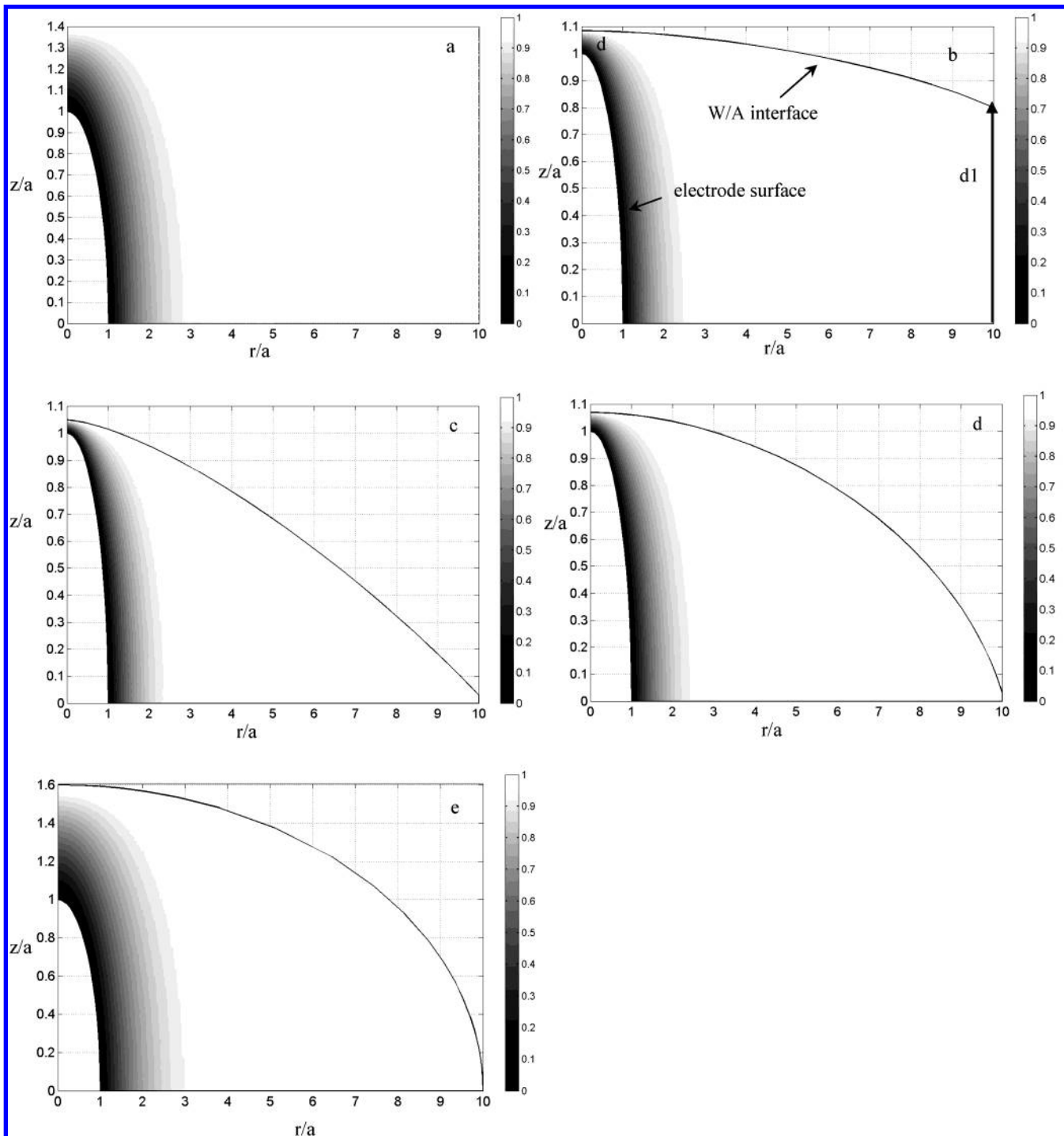


Figure 11. Simulated oxygen-concentration profiles (normalized with respect to the bulk value, scale bar of 0–1) for the geometries corresponding to the points labeled a–e in Figure 8. The calculations refer to a hemispherical microelectrode near a clean A/W interface.

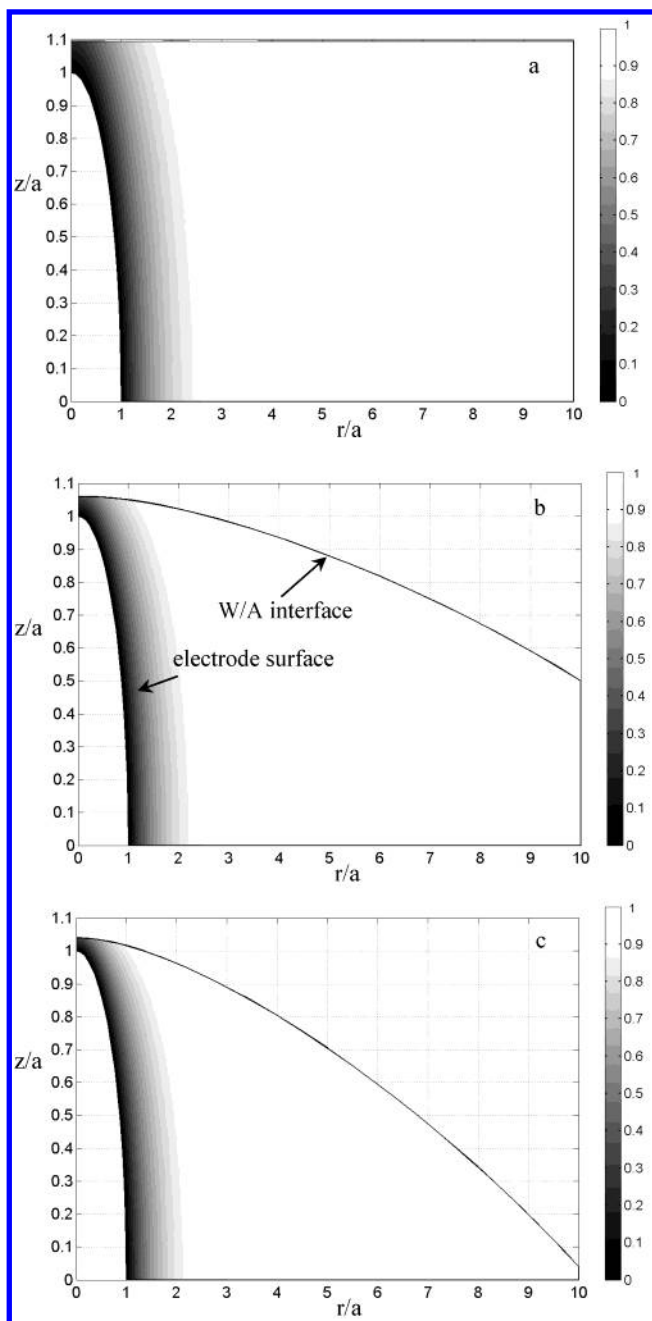


Figure 12. Simulated oxygen-concentration profiles (normalized with respect to the bulk value, scale bar of 0–1) for the geometries corresponding to the points labeled a–c in Figure 9a. The calculations refer to a hemispherical microelectrode near an A/W interface with a monolayer. The transfer rate constants used to generate the results were $k_{wa}/\text{cm s}^{-1} = 0.05, 0.143, \text{ and } 0.210$ for plots a, b, and c, respectively.

correction due to the perturbation of the surface. The last points, referring to the third regime (Figure 11d and e), consider a geometry where the water surface develops a singularity, and as a consequence, its stable shape is that of a sphere cap with a larger volume above the electrode plane (Figure 11e). In this latter case, the real closest distance between the tip and interface reaches about $0.7a$. This causes a decrease in the current. Finally, of course, the current drops to zero as soon as the electrode protrudes completely from the solution (data not shown).

The agreement between the numerical and experimental data is very close, indicating the veracity of our interpretation of the deformation process. This evaluation is consistent with the picture obtained by microscopy visualization of the process that occurs as the microelectrode emerges across the A/W interface.

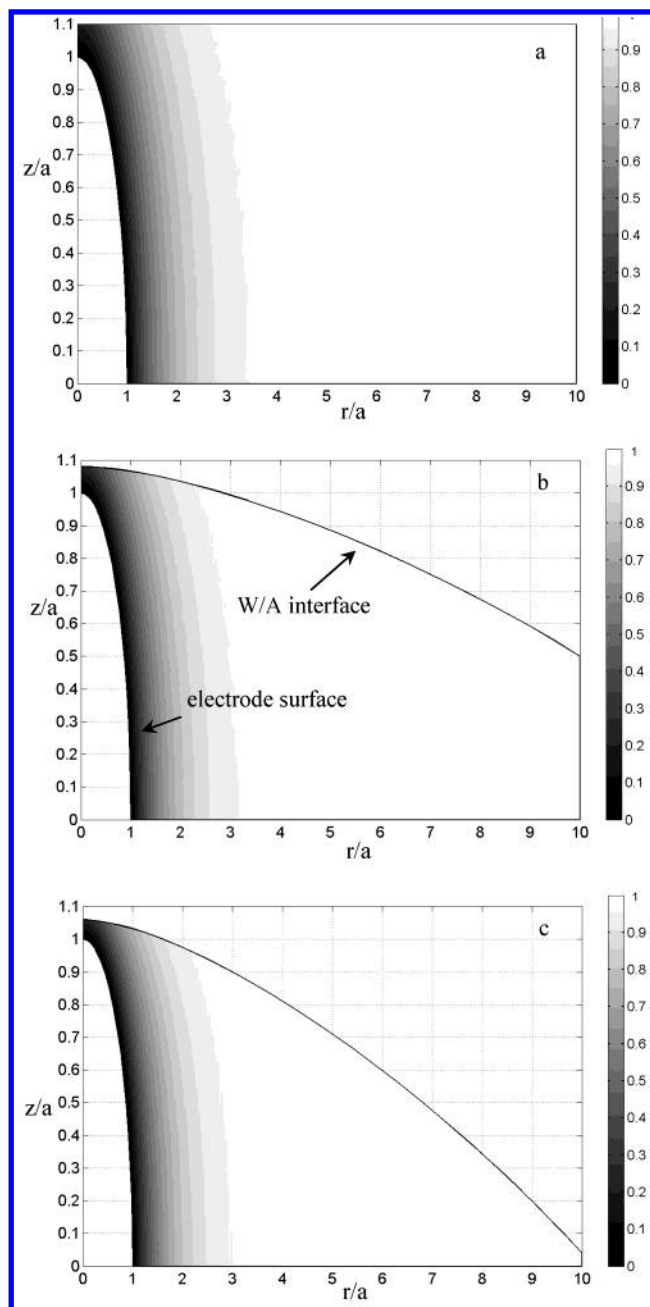


Figure 13. Simulated oxygen-concentration profiles (normalized with respect to the bulk value) for the geometries corresponding to the points labeled a–c in Figure 9b. The calculations refer to a hemispherical microelectrode near an A/W interface with a monolayer. The transfer rate constants used to generate the results were $k_{wa}/\text{cm s}^{-1} = 0.04, 0.064, \text{ and } 0.082$ for plots a, b, and c, respectively.

Deformation at an Interface with a DPPA Monolayer. Let us now consider the case in which the interface contains a DPPA monolayer. Figure 9 shows the experimental and numerical data corresponding to two different values of Π . Both curves were compared with numerical simulations up to $d/a = 0.09$ by considering a flat water interface. (See Figures 12a and 13a). At close distances, the deformation of the interface becomes important, as for the clean interface case, discussed in the preceding section. It is interesting that in all cases, with or without a monolayer, the deformation process starts to occur at a similar value of d/a , confirming our earlier work,¹⁸ but that thereafter the nature of the deformation depends on the interfacial tension. With a monolayer present, which lowers the

surface tension, there is a linear increase in the current that extends to a wide region of d/a . (See Figures 12b and c and 13b and c.)

By using the FEMLAB simulations, the observed increase in current could not be accounted for by simply allowing a smaller normalized distance, d/a , as invoked to explain the clean interface case. This was more evident at higher pressure ($\Pi = 30$ mN/m). As a result, the simulations performed to explain the deformation considered both a variable geometry (d/a and curvature) and variable kinetics of O_2 transfer. Thus, the observed current enhancement could be explained only if the rate constant, k_{wa} , increased in this second regime. This is reasonable because the tip-induced perturbation is likely to lead to more disorder within the DPPA monolayer, particularly in regions of higher curvature.

The resulting simulations for the DPPA case are in good agreement with the experimental data. The numerical calculations corresponding to the curve at $\Pi = 30$ mN/m were obtained by considering that the closest normalized approach distance was $d/a = 0.07$, and a variable rate constant (from 0.0403 to 0.114 $cm\ s^{-1}$) was employed. To fit the curve with $\Pi = 10$ mN/m, the minimum normalized distance was 0.03 a , and the rate constant increased from 0.0528 to 0.28 $cm\ s^{-1}$. Note that this analysis treats the whole interface as having a uniform rate constant. In reality, the perturbation effect will be most pronounced at the part of the interface directly above the tip and less important further away. However, it is the part of the interface nearest the tip that mainly influences the current (as evident from the oxygen-concentration profiles in Figures 12c and 13c), so this simple treatment is reasonable.

Conclusions

The effect of the surface pressure of $C_{18}OH$ and DPPA monolayers on the kinetics of O_2 transfer across the W/A interface has been investigated using a hemispherical mercury microelectrode as an SECM probe. The kinetic data extracted from the comparison between experimental and simulated data have been analyzed using the energy-barrier model,²² yielding a pore radius of 1.3–1.4 Å, consistent with the dimensions of O_2 .⁴⁴

During SECM approach-curve measurements, the W/A interface ultimately undergoes mechanical deformation (at close separations). The experimental current–distance curves display a reproducible behavior, depending on whether the interface is clean or has a monolayer. By fitting these approach curves with simulated data, it has been possible to develop a model for the tip-induced surface deformation process. For the case where there is a monolayer at the interface, the surface deformation impacts the order within the monolayer, and in turn, this causes an increase in the oxygen-transfer rate constant.

The detailed information in this paper on the nature of the approach curves recorded with a hemispherical electrode at a water surface will be useful for future studies. For example, we propose to carry out studies of metal ion uptake at a monolayer using the SECM setup coupled with anodic stripping voltammetry. Mercury microelectrodes offer additional prospects for SECM, including a greatly expanded cathodic window for amperometric detection, particularly in aqueous solution.

Acknowledgment. I.C. gratefully acknowledges scholarships from the MURST (Rome) and the Marie Curie training scheme (HMPT-CT-2001-00356). D.P.B. is supported by an EPSRC DTA studentship. Helpful discussions with Dr. J. V. Macpherson and Dr. J. Guo are much appreciated.

References and Notes

- (1) See, for example, (a) Adamson, A. W. *Physical Chemistry of Surfaces*; Wiley: New York, 1997. (b) Atherton, J. H. *Res. Chem. Kinet.* **1994**, 2, 193. (c) Benjamin, I. *Chem. Rev.* **1996**, 96, 1449.
- (2) See, for example, (a) Volkov, A. G.; Deamer, D. W.; Tanelian, D. L.; Markin, V. S. *Liquid Interfaces in Chemistry and Biology*; Wiley: New York, 1998. (b) Gennis, R. B. *Biomembranes*; Springer: New York, 1995.
- (3) See, for example, (a) Thibodeaux, L. J. *Environmental Chemodynamics: Movements of Chemicals in Air, Water and Soil*, 2nd ed.; Wiley: New York, 1996. (b) Schwarzenbach, R. P.; Gschwend, P. M.; Imboden, D. M. *Environmental Organic Chemistry*; Wiley: New York, 1993.
- (4) (a) Stein, W. D. *Transport and Diffusion across Cell Membranes*; Academic Press: San Diego, CA, 1986. (b) Speelmans, G.; Staffhorst, R. W. H. M.; De Wolf, F. A.; De Kruijff, B. D. *Biochim. Biophys. Acta* **1995**, 1238, 137. (c) Eytan, G. D.; Regev, R.; Oren, G.; Assaraf, Y. G. *J. Biol. Chem.* **1996**, 271, 12897.
- (5) (a) Othmer, H. G.; Buckhold Shank, B. *Math. Biosci.* **1977**, 34, 131. (b) Levitt, D. G.; Elias, S. R.; Hautman, J. M. *Biochim. Biophys. Acta* **1978**, 512, 436. (c) Deamer, D. W.; Bramhall, J. *Chem. Phys. Lipids* **1986**, 40, 167.
- (6) (a) Chem, Q.-P.; Li, Q.-T. *Arch. Biochem. Biophys.* **2001**, 389, 201. (b) Zeng, J.; Smith, K. E.; Chang, P. L.-G. *Biophys. J.* **1993**, 65, 1404. (c) Porter, K. K.; Brand, M. D. *Nature* **1993**, 362, 628. (d) Brand, M. D.; Chien, L. F.; Ainscow, E. K.; Rolfe, D. F. S.; Porter, R. K. *Biochim. Biophys. Acta* **1994**, 1187, 301.
- (7) (a) Haydon, D. A.; Hladky, B. S. *Quart. Rev. Biophys.* **1972**, 5, 187. (b) *Membranes: A Series of Advances*; Ciani, S. M., Eisenman, G., Laprade, R., Szabo, G., Eisenman, G., Eds.; Marcel Dekker: New York, 1973; p 2. (c) Tien, H. T. *Bilayer Lipid Membranes (BLM): Theory and Practice*; Marcel Dekker: New York, 1974. (d) Phillips, M. C.; Chapman, D. *Biochim. Biophys. Acta* **1968**, 163, 301.
- (8) (a) Brockman, H. *Curr. Opin. Struct. Biol.* **1999**, 9, 438. (b) MacDonald, R. C. In *Vesicles*; Rosoff, M., Ed.; Marcel Dekker: New York, 1996; pp 3–48. (c) Ferg, S. S.; Gong, K.; Chew, J. *Langmuir* **2002**, 18, 4061.
- (9) (a) Barnes, G. T.; Hunter, D. S. *J. Colloid Interface Sci.* **1990**, 136, 198. (b) Seaver, M.; Peele, J. R.; Manuccia, T. J.; Rubel, G. O.; Ritchie, G. J. *Phys. Chem.* **1992**, 96, 6389. (c) Drummond, C. J.; Elliot, P.; Furlong, D. N.; Barnes, G. T. *J. Colloid Interface Sci.* **1992**, 151, 189. (d) La Mer, V. K. *Retardation of Evaporation by Monolayers*; Academic Press: New York, 1962.
- (10) Rideal, E. K. *J. Phys. Chem.* **1925**, 29, 1585.
- (11) For reviews of SECM, see, for example, (a) Bard, A. J.; Fan, F.-R. F.; Pierce, D. T.; Unwin, P. R.; Wipf, D. O. *Science* **1991**, 254, 68. (b) Bard, A. J.; Mirkin, M. V.; Fan, F.-R. F. *Electroanal. Chem.* **1993**, 18, 243. (c) Mirkin, M. V. *Anal. Chem.* **1996**, 68, 177A. (d) Barker, A. L.; Gonsalves, M.; Macpherson, J. V.; Slevin, C. J.; Unwin, P. R. *Anal. Chim. Acta* **1999**, 385, 223. (e) Horrocks, B. R. In *Encyclopedia of Electrochemistry*; Bard, A. J., Stratman, M., Eds.; Wiley-VCH: Weinheim, Germany, 2002; Vol. 3 (Unwin, P. R., Ed.), p 444.
- (12) (a) Tsionsky, M.; Bard, A. J.; Mirkin, M. V. *J. Am. Chem. Soc.* **1997**, 119, 10785. (b) Delville, M. H.; Tsionsky, M.; Bard, A. J. *Langmuir* **1998**, 14, 2774. (c) Zhang, J.; Unwin, P. R. *J. Electroanal. Chem.* **2000**, 494, 47. (d) Zhang, J.; Unwin, P. R. *Langmuir* **2002**, 18, 2313. (e) Strutwolf, J.; Zhang, J.; Barker, A. L.; Unwin, P. R. *Phys. Chem. Chem. Phys.* **2001**, 3, 5553. (f) Zhang, J.; Strutwolf, J.; Cannan, S.; Unwin, P. R. *Electrochem. Commun.* **2003**, 5, 105.
- (13) (a) Amemiya, S.; Bard, A. J. *Anal. Chem.* **2000**, 72, 4940. (b) Tsionsky, M.; Zhou, J. F. Amemiya, S.; Fan, F.-R. F.; Bard, A. J.; Dryfe, R. A. W. *Anal. Chem.* **1999**, 71, 4300. (c) Shiku, H.; Takeda, T.; Yamada, H.; Matsue, T.; Uchida, I. *Anal. Chem.* **1995**, 67, 312.
- (14) (a) Uitto, O. D.; White, H. S. *Anal. Chem.* **2001**, 73, 533. (b) Bath, B. D.; Lee, R. D.; White, H. S.; Scott, E. R. *Anal. Chem.* **1998**, 70, 1047. (c) Scott, E. R.; White, H. S.; Phipps, J. B. *J. Membr. Sci.* **1991**, 58, 71.
- (15) (a) Yasukawa, T.; Kaya, T.; Matsue, T. *Electroanalysis* **2000**, 12, 653. (b) Yasukawa, T.; Kondo, Y.; Uchida, I.; Matsue, T. *Chem. Lett.* **1998**, 767.
- (16) Barker, A. L.; Macpherson, J. V.; Slevin, C. J.; Unwin, P. R. *J. Phys. Chem. B* **1998**, 102, 1568.
- (17) (a) Unwin, P. R.; Bard, A. J. *J. Phys. Chem.* **1992**, 96, 5035. (b) Macpherson, J. V.; Unwin, P. R. *J. Phys. Chem.* **1994**, 98, 1704.
- (18) Slevin, C. J.; Ryley, S.; Walton, D. J.; Unwin, P. R. *Langmuir* **1998**, 14, 5331.
- (19) (a) Slevin, C. J.; Unwin, P. R. *J. Am. Chem. Soc.* **2000**, 122, 2597. (b) Zhang, J.; Unwin, P. R. *J. Am. Chem. Soc.* **2002**, 124, 2379. (c) Zhang, J.; Unwin, P. R. *Phys. Chem. Chem. Phys.* **2002**, 4, 3814.
- (20) Zhang, J.; Unwin, P. R. *Langmuir* **2002**, 18, 1218.
- (21) (a) Zhang, J.; Slevin, C. J.; Morton, C.; Scott, P.; Walton, D. J.; Unwin, P. R. *J. Phys. Chem. B* **2001**, 105, 11120. (b) Quinn, B. M.; Prieto, I.; Haram, S. H.; Bard, A. J. *J. Phys. Chem. B* **2001**, 105, 7474. (c) Mandler, D.; Unwin, P. R. *J. Phys. Chem. B* **2003**, 107, 408. (d) Zhang, J.; Barker, A. L.; Mandler, D.; Unwin, P. R. *J. Am. Chem. Soc.* **2003**, 125, 9312.

- (22) (a) Langmuir, I.; Langmuir, D. B. *J. Phys. Chem.* **1927**, *31*, 1719. (b) Langmuir, I.; Schaefer, V. J. *J. Franklin Inst.* **1943**, *235*, 119. (c) Barnes, G. T.; Hunter, D. S. *J. Colloid Interface Sci.* **1990**, *136*, 198.
- (23) Cunnane, V. J.; Schifffrin, D. J.; Fleischmann, M.; Geblewicz, G.; Williams, D. *J. Electroanal. Chem.* **1988**, *243*, 455.
- (24) (a) Daniele, S.; Bragato, C.; Ciani, I.; Baldo, M. A. *Electroanalysis* **2003**, *15*, 621 and references therein. (b) Ciani, I.; Daniele, S.; Bragato, C.; Baldo, M. A. *Electrochem. Commun.* **2003**, *5*, 354.
- (25) (a) Failla, M. L.; Cousins, R. J. *Biochim. Biophys. Acta* **1978**, *538*, 435. (b) Pattison, S. E.; Cousins, R. J. *Am. J. Physiol.* **1986**, *250*, E677. (c) Reyes, J. G. *Am. J. Physiol.* **1996**, *270*, c401.
- (26) (a) Bos, M. A.; Nylander, T. *Langmuir* **1996**, *12*, 2791. (b) Zhao, W.; Kim, M. V.; Wurm, D. B.; Brittain, S. T.; Kim, Y. T. *Langmuir* **1996**, *12*, 386. (c) Eng, L. M.; Seuret, C.; Looser, H.; Günter, P. *J. Vac. Sci. Technol., B* **1996**, *14*, 1386. (d) DeMeijere, K.; Brezesinski, G.; Mohwald, H. *Macromolecules* **1997**, *30*, 2337. (e) Pack, D. W.; Arnold, F. H. *Chem. Phys. Lipids* **1997**, *86*, 135.
- (27) (a) Hauser, H.; Oldani, D.; Philips, M. C. *Biochemistry* **1973**, *12*, 4507. (b) Chesniuk, F. G.; Dassie, S. A.; Yudi, L. M.; Baruzzi, A. M. *Electrochem. Acta* **1998**, *43*, 2175.
- (28) Slevin, C. J.; Macpherson, J. V.; Unwin, P. R. *J. Phys. Chem. B* **1997**, *101*, 10851.
- (29) Kwak, J.; Bard, A. J. *Anal. Chem.* **1989**, *61*, 1221.
- (30) (a) Wehmeyer, K. R.; Wightman, R. M. *Anal. Chem.* **1985**, *57*, 1989. (b) Daniele, S.; Bragato, C.; Baldo, M. A.; Mazzocchin, G. A. *Ann. Chim. (Rome)* **2002**, *92*, 77.
- (31) Gericke, A.; Simon-Kutscher, J.; Huhnerfuss, H. *Langmuir* **1993**, *9*, 2119.
- (32) Kuchhal, Y. K.; Katti, S. S.; Biswas, A. B. *J. Colloid Interface Sci.* **1969**, *29*, 521.
- (33) (a) Pletcher, D.; Sotiropoulos, S. J. *J. Chem. Soc., Faraday Trans.* **1995**, *91*, 457. (b) Han, P.; Bartels, D. M. *J. Phys. Chem.* **1996**, *100*, 5597.
- (34) Selzer, Y.; Mandler, D. *Anal. Chem.* **2000**, *72*, 2383.
- (35) Amphlett, J. L.; Denuault, G. *J. Phys. Chem. B* **1998**, *102*, 9946.
- (36) Mirkin, M. V.; Fan, F.-R. F.; Bard, A. J. *J. Electroanal. Chem.* **1992**, *328*, 47.
- (37) Burnett, D. S. *Finite Element Analysis*; Addison-Wesley: Reading, MA, 1987.
- (38) (a) Miñones, J., Jr.; Rodríguez Patino, J. M.; Miñones, J.; Dynarowicz-Latka, P.; Carrera, C. *J. Colloid Interface Sci.* **2002**, *388*. (b) Luckham, P.; Wood, J.; Frogatt, S.; Wart, R. S. *J. Colloid Interface Sci.* **1996**, *153*, 368. (c) Girard-Egrot, A. P.; Morélis, R. M.; Coulet, P. R. *Langmuir* **1996**, *12*, 778. (d) Taylor, D. M.; Oliveira, O. N.; Morgan, H. *J. Colloid Interface Sci.* **1990**, *139*, 508. (e) Hauser, H.; Pasher, I.; Pearson, R. H.; Sundell, S. *Biochim. Biophys. Acta* **1981**, *650*, 21.
- (39) Zaitsev, S. Y.; Kalmer, U.; Mobius, D. *Colloids Surf., A* **1995**, *94*, 137.
- (40) Lundquist, M. *Chem. Scr.* **1971**, *1*, 5.
- (41) Barnes, G. T.; La Mer, V. K. In *Retardation of Evaporation by Monolayers*; La Mer, V. K., Ed.; Academic Press: New York, 1962; p 9.
- (42) (a) Archer, R. J.; La Mer, V. K. *J. Phys. Chem.* **1955**, *59*, 200. (b) La Mer, V. K.; Healy, T. W.; Aylmore, L. A. G. *J. Colloid Sci.* **1964**, *19*, 673.
- (43) Blank, M. *J. Phys. Chem.* **1962**, *66*, 1911.
- (44) *Book of Data (Chemistry, Physical Science, Physics)*; Harrison, R. D., Ed.; Nuffield Advance Science: London, 1980.